Glacial-Interglacial Indian Summer Monsoon Dynamics

An Zhisheng,[1,2]* Steven C. Clemens,[3] Ji Shen,[4] Xiaoke Qiang,[1] Zhangdong Jin,[1] Youbin Sun,[1] Warren L. Prell,[3] Jingjia Luo,[5] Sumin Wang,[4] Hai Xu,[1] Yanjun Cai,[1] Weijian Zhou,[1,2] Xiaodong Liu,[1] Weiguo Liu,[1] Zhengguo Shi,[1] Libin Yan,[1] Xiayun Xiao,[4] Hong Chang,[1] Feng Wu,[1] Li Ai,[1] Fengyan Lu[1]

The modern Indian summer monsoon (ISM) is characterized by exceptionally strong interhemispheric transport, indicating the importance of both Northern and Southern Hemisphere processes driving monsoon variability. Here, we present a high-resolution continental record from southwestern China that demonstrates the importance of interhemispheric forcing in driving ISM variability at the glacial-interglacial time scale as well. Interglacial ISM maxima are dominated by an enhanced Indian low associated with global ice volume minima. In contrast, the glacial ISM reaches a minimum, and actually begins to increase, before global ice volume reaches a maximum. We attribute this early strengthening to an increased cross-equatorial pressure gradient derived from Southern Hemisphere high-latitude cooling. This mechanism explains much of the nonorbital scale variance in the Pleistocene ISM record.

The Indian summer monsoon (ISM), as an important component of the global monsoon system, is driven by cross-equatorial pressure gradient (XEPG) between the Indian low over the Asian continent and the Mascarene high in the southern Indian Ocean (Fig. 1A) (1, 2). This is a uniquely coupled, bi-hemispheric system; nowhere else on Earth does cross-equatorial transfer of heat and momentum compare in magnitude or meridional extent. The Indian low is driven both by direct sensible heating of the Asian continent, particularly the Tibetan Plateau, and by subsequent latent heat release due to moisture supply from the Indian Ocean (2, 3). The Mascarene high is forced by the subsiding branch of the Southern Hemisphere (SH) Hadley cell owing to the Equator-to-Antarctica temperature gradient and can be enhanced during the development of monsoonal circulation (4).
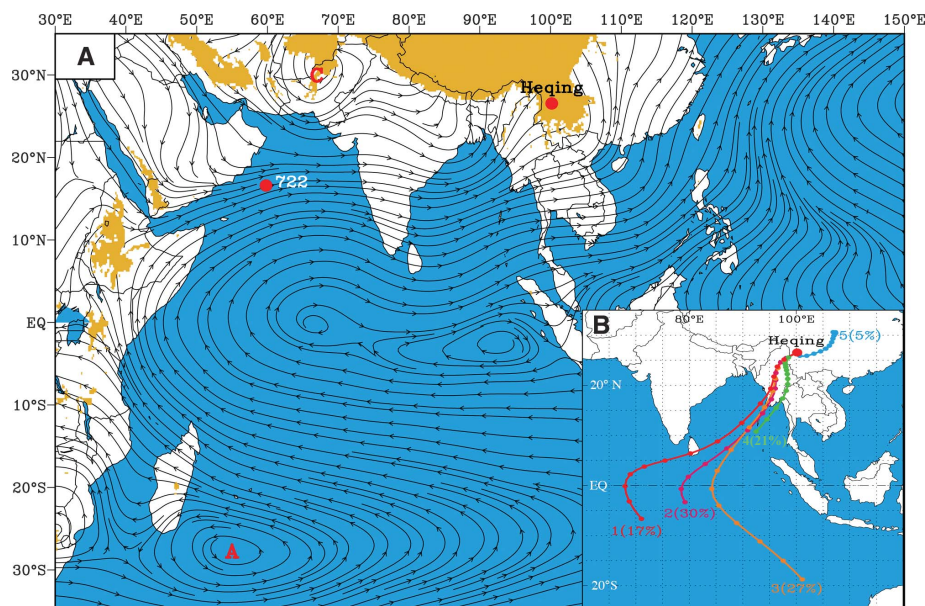
Heqing Basin is located in Yunnan Province, southwestern China, near the southeastern edge of the Tibetan Plateau (Fig. 1A). The local climate is entirely monsoonal, characterized by warm wet summers and cool dry winters (figs. S1 and S2). The Indian Ocean is the major moisture source at present (Fig. 1B) and probably during the last glacial maximum (LGM) (fig. S3) (5). In 2002, a 666-m-long sediment core (26°33′43″N, 100°10′14″E, 2190 m above sea level) was retrieved from the central part of the Heqing paleolake basin (fig. S4) with 97% recovery (6). The lake sediments mainly consist of horizontally laminated grayish-green calcareous clay and silty clay with thin-bedded silt and fine sand layers, except for two intervals of sand layers with fine gravels (6). Aqueous herb pollen (*Myriophyllum* and *Sparganium*) (7) are found throughout the core, indicating that the sediments are of typical lacustrine origin.

An abrupt drop in $\delta^{18}O$ (a measure of the ratio of stable isotopes $^{18}O{:}^{16}O$) (fig. S5) and a shift in the relationship between $\delta^{18}O$ and $\delta^{13}C$ (a measure of the ratio of stable isotopes $^{13}C{:}^{12}C$) (fig. S6) of adult ostracod *Ilyocypris microspinata* shells around 11.1 m probably indicate the beginning of a change from a closed paleolake to an open system [supporting online material (SOM) text]. At 7.4 m depth, the simultaneous disappearance of two benthic ostracod species (*Ilyocypris microspinata* and *Lineocypris jiangsuensis*) indicates that the basin became a fully open system as it is today. Accordingly, we focus on the interval when the system was closed.

Proxies and chronology. Samples at 10- to 20-cm intervals over the upper 200 m depth (~900-year resolution) and 50-cm intervals below 200 m (~2000-year resolution) were analyzed for proxies, including total organic carbon (TOC), Rb/Sr, and pollen (Fig. 2). In the study of paleoclimatic change, it is well accepted that TOC of the lake sediments is closely related to the biomass (8, 9), which is affected by precip-

[1]State Key Laboratory of Loess and Quaternary Geology, Institute of Earth Environment, Chinese Academy of Sciences, Xi'an 710075, China. [2]Institute of Global Environmental Change, Xi'an Jiaotong University, Xi'an 710049, China. [3]Department of Geological Sciences, Brown University, Providence, RI 02912, USA. [4]Nanjing Institute of Geography and Limnology, Chinese Academy of Sciences, Nanjing 210008, China. [5]Research Institute for Global Change, Japan Agency for Marine-Earth Science and Technology, Kanagawa 236-0001, Japan.

*To whom correspondence should be addressed. E-mail: anzs@loess.llqg.ac.cn

Fig. 1. (**A**) June-July-August (JJA) mean 850 hPa streamline based on the National Centers for Environmental Prediction/National Center for Atmospheric Research reanalysis (52) during 1971–2000. Red dots denote the locations of Heqing and ODP site 722, "A" indicates the center of the Mascarene high, and "C" indicates the center of the Indian low. Areas above 1500 m (above sea level) are shaded in yellow. (**B**) Moisture source for JJA precipitation at Heqing, represented by five typical groups of 14-day backward trajectory analysis of air-flow at 100 m height above surface. These were calculated by using the HYSPLIT v4.8 model (53), with a time interval of one day between marks, reflecting different velocities. Similar trajectories were merged through cluster analysis with 1840 samples in total (1991–2000, JJA, sampled twice per day at UTC06 and UTC18). The results indicate that more than 90% of total moisture for summer precipitation at Heqing comes from the Indian Ocean.

itation and temperature in the monsoon regions (9, 10). In boreal summer, the ISM, which is characterized by high temperature and precipitation, leads to increased biomass within the catchment and increased lake productivity due to favorable hydrological conditions and a rich nutrient supply. These conditions result in increased sedimentary TOC, integrating the terrestrial and aquatic organic matter (8). High correlation [correlation coefficient (r) = 0.69] between sedimentary TOC and the carbon/nitrogen (C/N) ratio confirms that the changes of sedimentary TOC content depend on the input of terrestrial organic matter (figs. S7 and S8) (6). Thus, TOC captures the timing and amplitude of strong summer monsoon events. However, it is truncated at low values (Fig. 2), suggesting that it does not document the true extent of weak summer monsoons.

Rubidium (Rb) is incorporated mainly in potassium (K)–bearing silicates and displays inert geochemical behavior, whereas strontium (Sr) substitutes for calcium (Ca) in the lattices of carbonates. During intervals of strong monsoons, carbonate weathering dominates, especially in the Heqing basin, which is predominantly limestone, resulting in low Rb/Sr ratios in sediments (11). During times of weak monsoons, carbonate weathering decreases in this transport-limited region, yielding a high Rb/Sr ratio. Similar to the TOC proxy, Rb/Sr is truncated at low values (strong weathering), approaching values as low as 0.1. Therefore, Rb/Sr better captures the amplitude of weak events but not strong ones. The chemical index of alteration (CIA) is a measure of the proportion of aluminum oxide (Al_2O_3) versus the labile oxides ($Na_2O+K_2O+CaO^*$), where CaO^* is the amount of CaO incorporated in the silicate fraction (12). The CIA and Rb/Sr records are highly correlated (r^2 = 0.743), further supporting the interpretation of the Rb/Sr ratio as a weathering proxy (fig. S9) (6). Given the in-phase relationship (table S1) and "back-to-back" pattern between Rb/Sr and TOC (Fig. 2), we combined the two records by normalizing each to unit variance and averaging to produce a stacked ISM index that captures the full amplitude of variability. We interpret the ISM index as most indicative of summer monsoon variability, with high values indicating enhanced ISM circulation.

Pollen analysis shows strong *Tsuga* variability in the Heqing lake sediment sequence (7). *Tsuga* flourishes under warm and humid conditions, with moderate temperature ranges at elevations of 2000 to 3500 m in southeastern Asia (13). A necessary condition for overwintering of the thermophilic *Tsuga* is an annual temperature range less than 22°C (14). Modern *Tsuga* in the Asian monsoonal area is distributed in the mountainous regions of southwest China, southeast China, central China, Taiwan Island, and the south-central part of Japan (fig. S10). Moisture conditions within these monsoonal regions generally meet *Tsuga* growth requirements in mountainous regions. However, annual mean temperature (5.8 to 18.2°C), especially winter mean temperature

(–2.7 to 11.5°C), and annual temperature range (9.7 to 25.4°C) become limiting factors for *Tsuga*, as indicated by analysis of the modern geographical distribution of *Tsuga* in monsoonal regions (SOM text and table S2) (15). Thus, *Tsuga* is primarily sensitive to winter temperature and annual temperature range. Simulations indicated that winter temperature decreased and annual temperature range increased in southwestern China during the LGM (5), presumably constraining *Tsuga* geographically. *Tsuga* is presently found in the south of the Qinling Mountains (~33°N) under modern warm conditions. It extended northward into northern China and even sparsely into the coastal areas of northeastern China (16, 17) during the Holocene Optimum, a time that was 2 to 3°C warmer than present (14). Therefore, Heqing core intervals with low or zero *Tsuga* pollen content are associated with LGM-like conditions, whereas those with high *Tsuga* content correspond to warm, interglacial periods.

Correlation of the Heqing magnetic polarity sequence with a geomagnetic polarity time scale (18–20) indicates that the core records the Brunhes, Matuyama, and late Gauss chrons, the Jaramillo and Olduvai subchrons, as well as

some geomagnetic excursions (Fig. 2, SOM text, and fig. S11). The reversal near 4.5 m indicates the Laschamp excursion event (20) as corroborated with accelerator mass spectrometry ^{14}C dating [~42 thousand years ago (ka)] (fig. S12).

Considering that the Laschamp excursion event is located near 4.5 m (fig. S12), high *Tsuga* content from 11.1 to 7.4 m corresponds to the last interglacial interval (fig. S5). Thus, 11.1 m is assigned as termination II (129.8 ka). Most of the high *Tsuga* intervals are clearly associated with ice volume minima when plotted on a time scale derived from linear interpolation between the Brunhes/Matuyama boundary and termination II (fig. S13). On the basis of this association and the link between *Tsuga* range and winter temperatures, we developed a refined astronomical time scale by simultaneously tuning the 41- and 21-ky (thousand years) components of the *Tsuga* content to the earth-orbital obliquity and precession parameters (21). Over the past 1.5 million years (My), we incorporated the same lags as used in the late Pleistocene marine $\delta^{18}O$ chronology, 8 and 5 ky for obliquity and precession, respectively (22). Between 2.6 and 1.5 million years ago (Ma), we account for the decreasing
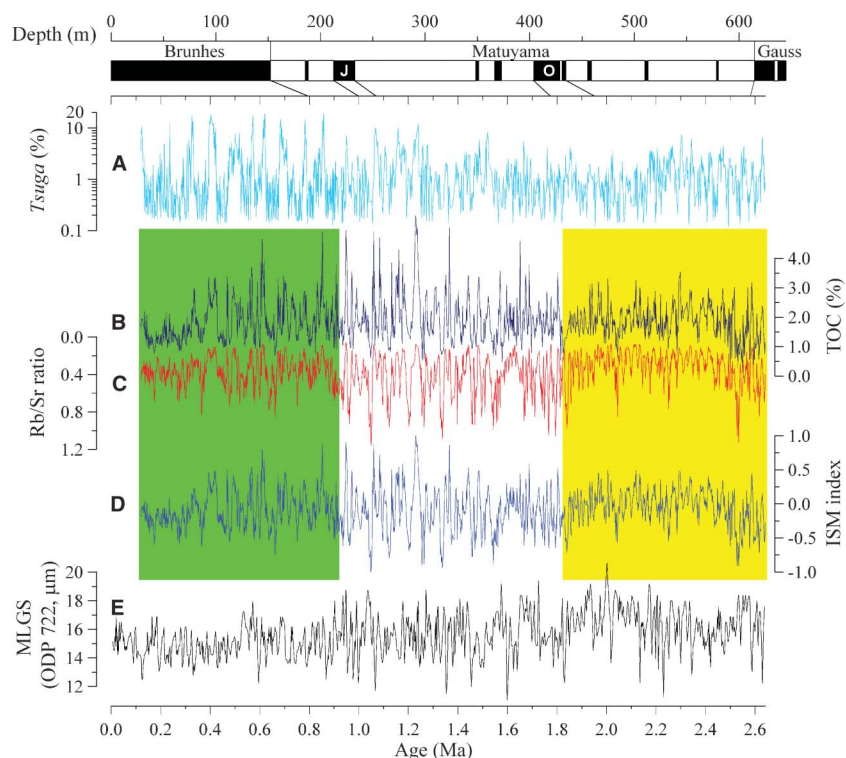
Fig. 2. Proxy ISM records since 2.60 Ma from Heqing Basin, southwest China. (**A**) Winter temperature proxy (*Tsuga*, percent) used for astronomical tuning. High value indicates high winter temperature (small annual temperature range). (**B**) Biologic productivity proxy TOC; high value represents strong summer monsoon. (**C**) Weathering proxy (Rb/Sr) for summer monsoon intensity, with low ratio (high Sr) reflecting strong monsoon. (**D**) Stacked ISM index from (B) and (C); high value indicates strong summer monsoon. (**E**) ISM intensity [ODP 722 median lithogenic grain size (MLGS)]; coarse size reflects strong monsoon (24). Middle interval (1.82 to 0.92 Ma) shows relatively large ISM amplitude, whereas the intervals before and after (green bar indicates 0.92 to 0.13 Ma, and yellow indicates 2.60 to 1.82 Ma) are characterized by relatively low amplitude. (Top) Paleomagnetic time sequence.

phase of $\delta^{18}O$ relative to orbital forcing by 2 ky at the obliquity band and by 0.7 ky at the precession band (SOM text and figs. S14 and S15) (*23*). This age model (Fig. 2) is supported by the observation that cross-spectral analyses of the ISM index with Ocean Drilling Program (ODP) 722 lithogenic grain size from the Arabian Sea (*24*) indicates high coherence and nearly in-phase relationships at the obliquity and precession bands (table S1). Given the continental location and the higher temporal resolution relative to ODP 722 proxies, our index provides a valuable record documenting ISM variability of the past 2.6 My.

0.92 to 0.13 million years ago. Previous studies of long-term ISM changes emphasized orbital- and/or tectonic-scale variability and mechanisms (*24–32*). Here, we focus on the influence of changing lower-boundary conditions on ISM circulation at the glacial-interglacial time scale. In particular, we concentrate on the timing of ISM maxima and minima relative to changes in northern hemisphere (NH) ice volume and Antarctic temperature. The fundamental relationships we seek to explain are illustrated in Fig. 3. Visual inspection reveals that there is much more structure in the Heqing ISM record than in ei-

ther the benthic $\delta^{18}O$ record, which is a proxy of global ice-volume change occurring mostly in the NH over the Pleistocene (*23*), or the Antarctic δD record, which is an indicator of high-latitude SH temperature change (*33*).

This relative complexity is clearly seen in spectra comparing these records (fig. S16); the Heqing ISM spectrum contains spectral peaks at 73-, 55-, and 29-ky periods, in addition to primary orbital periods associated with eccentricity (100 ky) and precession (23 and 19 ky). The obliquity period (41 ky) is insubstantial in the ISM index but is distinct in the *Tsuga* record, implying that the forcing mechanisms driving the ISM and *Tsuga* variability are not the same. Climatically, we attribute the relative complexity of the ISM spectrum to the combined influence of NH ice volume and SH temperature as described below.

During strong interglacials, ISM maxima coincide with NH ice volume minima and Antarctic temperature maxima (Fig. 3). From peak interglacials into glacials, the ISM weakens as ice volume increases (Fig. 3, light blue arrows). However, the weakening of the ISM into glacials is not smooth or linear; a number of strong "secondary" ISM peaks exist that have no correla-

tive structure in the $\delta^{18}O$ record (for example, Fig. 3, peaks "a" through "g"). Transitioning from interglacials into glacials, ISM strength reaches a minimum as benthic $\delta^{18}O$ achieves ~4.5 per mil (‰), corresponding to low, often minimum Antarctic temperatures (δD minima). These ISM minima occur 14 to 35 ky earlier than the timing of NH glaciation maxima. Similar leads are found in the 350-ky Summer Monsoon Stack from the northern Arabian Sea (SOM text and fig. S17) (*29*). Subsequently, the ISM strengthens gradually (Fig. 3, black arrows), even as NH ice volume continues to grow. Lastly, the ISM intensifies rapidly along with the glacial termination. ISM minima do not occur early during moderate glacial intervals. For example, during MIS 14 the ISM minimum is in phase with ice volume maximum.

A number of questions arise from these observations, including (i) what drives the timing of early ISM minima, (ii) what drives the increasing ISM intensity even as NH ice volume continues to grow, and (iii) what drives the secondary ISM maxima? We hypothesize that the early ISM minima and the slowly strengthening ISM that follows are linked to low SH temperatures as depicted by Antarctic δD (*33*), increasing Antarctic ice volume (*34*), and low sea surface temperatures (SSTs) (Fig. 3, pink curve) (*35*).

To explain this link mechanistically, we noted that polar temperatures vary with greater amplitude than do tropical temperatures (*5*). During interglacials, ISM (XEPG) maxima are driven by an enhanced Indian low associated with both global ice volume minima and abundant moisture supply. Moving from peak interglacials into glacials, increasing NH glaciation decreases the strength of the Indian low. This is consistent with previous proxy studies (*29, 31, 36*) and numerical simulations (*26, 37*), indicating a weakening of the ISM with the growing NH ice sheets. However, ISM minima occur when NH glaciation reaches a level equivalent to ~4.5‰ in the benthic $\delta^{18}O$ record and Antarctic temperatures are near their lowest. Subsequently, ISM strength begins to slowly increase even as glaciation continues to build, and the moisture supply is relatively low (*38*). This glacial ISM strengthening can be attributed to an increasing XEPG resulting from the low Antarctic temperature (Fig. 3) (*33*) and increasing Antarctic ice volume (fig. S18) (*34*), which lead to enhanced SH atmospheric meridional circulation and a strengthened Mascarene high. We propose that this dynamical SH forcing more than compensates for the effects of increased NH glaciation, which serves to weaken the Indian low. This SH forcing has been suggested to explain Asian monsoon climate events during the last glaciation (*39–41*). Modern observations also show that colder-than-normal Antarctic temperatures lead to a stronger Mascarene high, which tends to strengthen the cross-equatorial Somali jet (*42*) and the ISM.
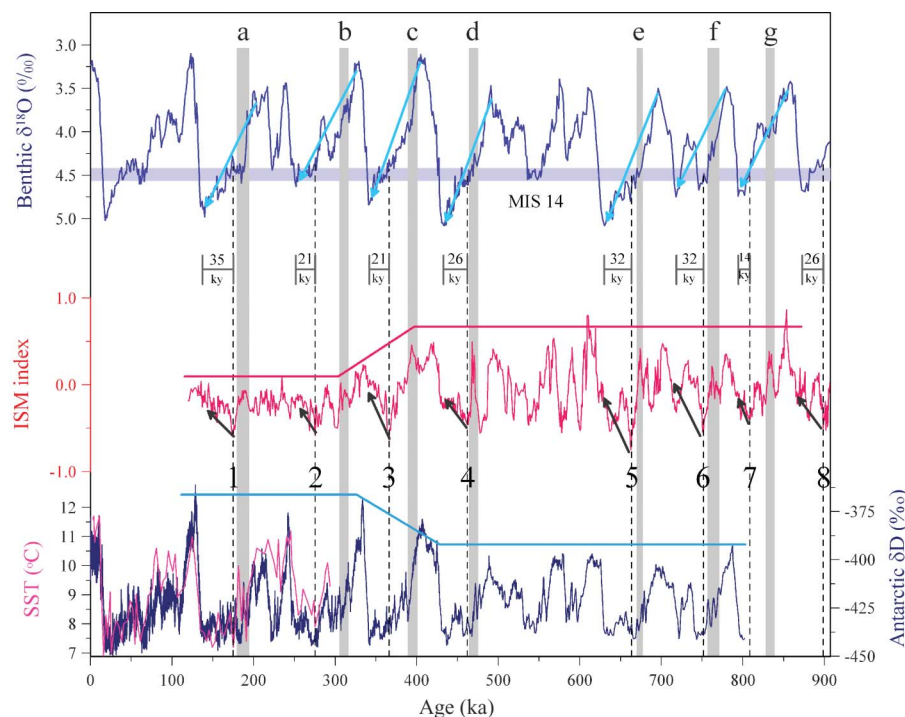
Fig. 3. Comparison between Heqing ISM index (red), global ice volume (blue, benthic $\delta^{18}O$, LR04 age scale) (*23*), and Antarctic deuterium (dark blue, EDC δD, EDC3 age scale) (*33*) during the past 900 ky. The mid-latitude southern hemispheric SST (pink, RC11-120) (*35*) varies simultaneously with Antarctic temperature. The horizontal gray bar in the benthic $\delta^{18}O$ shows a ~4.5‰ threshold. ISM minima lead global ice volume maxima by 14 to 35 ky. The black dashed vertical lines show the minima of the ISM, labeled from 1 to 8. The light blue arrows show the transition from interglacial to glacial, and the black arrows show strengthening ISM before global ice volume maxima. Secondary ISM peaks (gray shadings, "a" through "g") occur during the slow transition from interglacials into glacials. Thick solid red and sky-blue lines show the long-term amplitude relationship between ISM and Antarctic temperature.

Fig. 4. The timing of Heqing ISM minima relative to global ice volume maxima (benthic $\delta^{18}O$, LR04 age scale) (23) during the glacials within three intervals over the past 2.60 My. The red numbers and lines indicate times when ISM minima lead ice volume maxima, whereas the black numbers indicate in-phase relationships between the two. In the middle interval (1.82 to 0.92 Ma), most of ISM minima (17 of 19) are coincident with ice volume maxima, whereas in the young and old intervals most and half of ISM minima lead ice volume maxima, respectively.
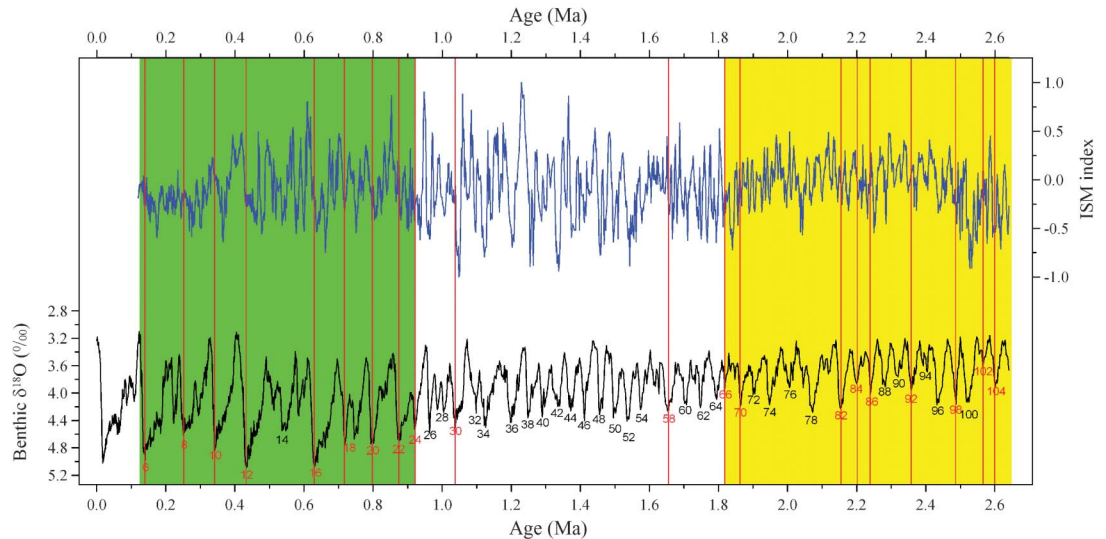
Fig. 5. Comparison of the Heqing ISM index (red) with IRD (blue) from ODP 907 (45) and their filtered and cross-spectral results for three intervals: (**A**) 0.92 to 0.13 Ma, (**B**) 1.82 to 0.92 Ma, and (**C**) 2.60 to 1.82 Ma. The ISM and IRD spectra are plotted on arbitrary log scales. The coarse dashed lines are the coherency spectra plotted on hyperbolic arctangent scales. Shaded bars indicate the dominant spectral peaks for these two records and high coherence at obliquity and precession bands. Band-pass filters with central frequencies of 0.0244 and 0.0476 ky^{-1} and bandwidths of 0.003 and 0.006 ky^{-1} are used to isolate the 41- and 21-ky components, respectively, of the IRD and ISM time series. Strong coherency and amplitude match between the two records, particularly at the 41-ky band over 1.82 to 0.92 Ma, indicates a dominant NH forcing that results in large-amplitude fluctuations of the ISM variation.
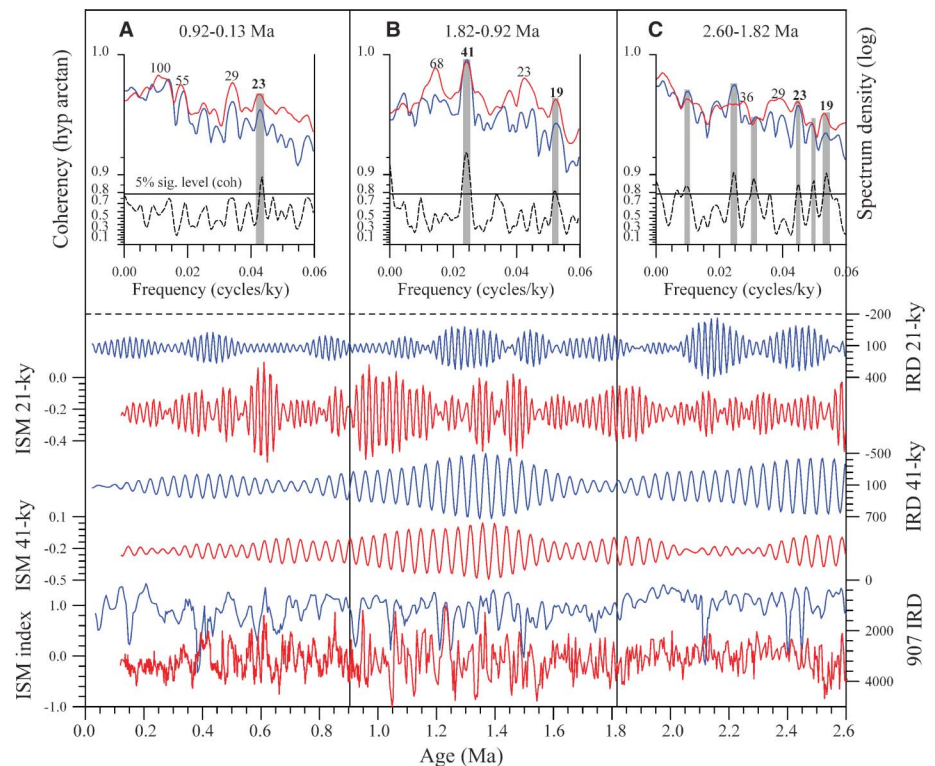
When global ice volume decreases and passes the threshold of ~4.5‰ into interglacial time, the continental Indian low rapidly intensifies and thus enhances the XEPG and ISM, together with an increased moisture supply from the warming tropical Indian Ocean. Meanwhile, the Intertropical Convergence Zone moves northward (43).

Interglacial ISM peaks that are in phase with NH ice volume minima are interpreted as responding to dominance of the enhanced Indian low, in spite of a simultaneously increased Antarctic temperature that acts to weaken the south-

ern ocean high. Analyses of simulated sea-level pressure show the strengthened Indian low and ISM in mid-Holocene (30), which illustrates the remarkable northern influence on the interglacial XEPG. Even so, the effect of a weaker southern high can be seen in ISM amplitude variations during interglacials. For example, the amplitude of ISM maxima is decreased in the interval from 0.40 to 0.13 Ma relative to the 0.80 to 0.43 Ma interval (Fig. 3, red line). This decrease cannot be ascribed to the weakening of the northern low, given that ice volume minima actually enhance slightly within this interval. We attribute

the decreased amplitude of interglacial ISM maxima to relatively high Antarctic temperatures. Similarly, increased amplitude of the interglacial ISM can be interpreted as responding to relatively low Antarctic temperatures from 0.80 to 0.43 Ma (33).

As noted previously, the decrease in ISM strength from peak interglacials into glacials is not linearly related to the increase in ice volume. Secondary ISM peaks occur during the slow transition from interglacials into glacials and generally correlate with low values of Antarctic temperatures (Fig. 3, peaks "a" through

"f"). It is plausible that the secondary peaks result from the combined influence of NH ice volume and SH temperature change, which is consistent with large concentrations of variance at nonprimary orbital periods (such as 29, 55, and 73 ky) in the ISM spectrum (SOM text and fig. S16).

ISM variations are closely linked to interaction between NH and SH dynamic processes during the past 0.92 My. Within this interval, increased glacial ice volume in both hemispheres as indicated by both proxy (23) and modeling results (34) supports our interpretation of ISM variability. At the glacial-interglacial time scale, ISM intensity can be thought of as being enhanced dominantly by northern low pressure during interglacials and dominantly by southern high pressure during glacials (fig. S19, illustration).

1.82 to 0.92 and 2.60 to 1.82 million years ago. On the basis of the phase relationship between ISM minima and $\delta^{18}O$ maxima (Fig. 4), the ISM record is separated into three intervals: 0.92 to 0.13, 1.82 to 0.92, and 2.60 to 1.82 Ma. In the middle interval, 17 of the 19 ISM minima are coincident with ice volume maxima. In contrast, nine of the 18 ISM minima in the older interval lead ice volume maxima by an average of 19 ky. Extrapolating our interpretation of mechanisms operating in the younger interval, we suggest that during the middle interval the northern low is dominant, whereas both the southern high and northern low forcings are active during the older interval.

This interpretation is supported by the long-term changes in ISM amplitude. Within the older and younger intervals, the ISM record exhibits relatively low amplitude, whereas within the middle interval it shows enhanced amplitude (Figs. 2 and 4). Lower amplitude variability within the younger and older intervals results from both the southern high and northern low forcings operating at the same time; when one is strong, the other is weak, serving to diminish XEPG and ISM amplitude. In further support of both the southern high and northern low forcings operating during the older interval, increased NH ice volume from 2.6 to 1.8 Ma (23) probably co-occurred with the expansion of Antarctic sea ice and decreased southern ocean SST, as can be inferred from southern ocean records (44). Within the middle interval, the northern low dominates as reflected by the in-phase relationship between NH ice volume and the ISM index, resulting in enhanced ISM amplitude (Fig. 5). Further support for the northern low dominance within the middle interval stems from high coherence between the ISM index and ice volume at all three orbital bands (table S1 and fig. S20) and the close relationship between the ISM and the North Atlantic IRD (ice-rafted debris) record (45) during the middle interval at the obliquity band (Fig. 5). Mechanistically, strengthened North Atlantic cold intervals marked by IRD events can weaken the ISM (46) by reducing land-ocean thermal gradient (47), in-

creasing Tibetan Plateau snow cover (48), and strengthening the westerly jet (49).

The hypothesis we put forth focuses on constraints of ice volume and Antarctic temperature on the timing of ISM (XEPG) changes during the Pleistocene. Early strengthening of the ISM, before full glacial conditions, is attributed to strengthening of the XEPG in response to Antarctic cooling. External (insolation) and other internal factors (such as greenhouse gases) contribute to ISM changes as well. For example, the strong coupling between CO_2 and Antarctic temperature over the past 800 ky (50) highlights the potential influence of atmospheric CO_2 on ISM variability at the glacial-interglacial time scale as a direct radiative forcing, the effects of which may be amplified by positive feedbacks, contributing further to Antarctic temperature change (51). In any case, our data demonstrate that the changing ISM (XEPG) is driven by the relative dominance of the northern low- and southern high-pressure systems during the Pleistocene; both are indispensable for understanding monsoon dynamics.

References and Notes

1. R. A. Tomas, P. J. Webster, *Q. J. R. Meteorol. Soc.* **123**, 1145 (1997).
2. P. J. Webster, J. Fasullo, in *Encyclopedia of Atmospheric Sciences*, J. Holton, J. A. Curry, Eds. (Academic Press, London, 2003), pp. 1370–1385.
3. P. J. Webster, in *Monsoons*, J. S. Fein, P. L. Stephens, Eds. (Wiley, New York, 1987), pp. 3–32.
4. J. R. Holton, *An Introduction to Dynamic Meteorology* (Academic Press, London, 1992), pp. 310–381.
5. P. Braconnot et al., *Clim. Past* **3**, 261 (2007).
6. Materials and methods are available as supporting material on *Science* Online.
7. X. Xiao, J. Shen, S. Wang, H. Xiao, G. Tong, *Sci. China (D)* **50**, 1189 (2007).
8. P. A. Meyers, E. Lallier-Vergès, *J. Paleolimnol.* **21**, 345 (1999).
9. D. A. Hodell et al., *Quat. Res.* **52**, 369 (1999).
10. X. Q. Liu et al., *Earth Planet. Sci. Lett.* **280**, 276 (2009).
11. Z. D. Jin, J. Cao, J. Wu, S. M. Wang, *Earth Surf. Process. Landf.* **31**, 285 (2006).
12. H. W. Nesbitt, G. M. Young, *Nature* **299**, 715 (1982).
13. A. Farjon, *Pinaceae: Drawings and Descriptions of the Genera* Abies, Cedrus, Pseudolarix, Keteleeria, Nothotsuga, Tsuga, Cathaya, Pseudotsuga, Larix *and* Picea (Koeltz Scientific Books, Königstein, Germany, 1990), pp. 149–151.
14. Z. S. An et al., in *Loess, Quaternary Geology and Global Change (Part II)*, T. S. Liu, Ed. (Science Press, Beijing, 1990), pp. 1–26 (in Chinese).
15. Q. S. Yang, Y. W. Xing, Z. K. Zhou, *Acta Botanica Yunnanica* **31**, 389 (2009) (in Chinese with English abstract).
16. C. H. Jia, L. Yu, N. Q. Du, Z. C. Kong, *Scientia Geographica Sinica* **9**, 274 (1989) (in Chinese with English abstract).
17. Z. C. Kong, N. Q. Du, Q. H. Xu, G. B. Tong, in *Climate and Environment during Holocene Megathermal in China*. Y. F. Shi, Z. C. Kong, Eds. (China Ocean Press, Beijing, 1992), pp. 48–65 (in Chinese).
18. S. C. Cande, D. V. Kent, *J. Geophys. Res.* **100**, (B4), 6093 (1995).
19. J. E. T. Channell, A. Mazaud, P. Sullivan, S. Turner, M. E. Raymo, *J. Geophys. Res.* **107**, (B6), 491 (2002).
20. H. Guillou et al., *Earth Planet. Sci. Lett.* **227**, 331 (2004).
21. J. Laskar, F. Jouzel, F. Boudin, *Astron. Astrophys.* **270**, 522 (1993).
22. J. Imbrie et al., in *Milankovitch and Climate, Part 1*, A. L. Berger, et al., Eds. (Riedel, Hingham, MA, 1984) pp. 269–305.
23. L. E. Lisiecki, M. E. Raymo, *Paleoceanography* **20**, PA1003 (2005).
24. S. C. Clemens, D. W. Murray, W. L. Prell, *Science* **274**, 943 (1996).
25. S. C. Clemens, W. Prell, D. Murray, G. Shimmield, G. Weedon, *Nature* **353**, 720 (1991).
26. W. L. Prell, J. E. Kutzbach, *Nature* **360**, 647 (1992).
27. W. L. Prell, J. E. Kutzbach, in *Tectonic Uplift and Climate Change*, W. F. Ruddiman, Ed. (Plenum, New York, 1997), pp. 171–201.
28. Z. S. An, J. E. Kutzbach, W. L. Prell, S. C. Porter, *Nature* **411**, 62 (2001).
29. S. C. Clemens, W. L. Prell, *Mar. Geol.* **201**, 35 (2003).
30. Z. Liu, B. Otto-Bliesner, J. Kutzbach, L. Li, C. Shields, *J. Clim.* **16**, 2472 (2003).
31. S. C. Clemens, W. L. Prell, Y. Sun, Z. Liu, G. Chen, *Paleoceanography* **23**, PA4210 (2008).
32. J. E. Kutzbach, X. Liu, Z. Liu, G. Chen, *Clim. Dyn.* **30**, 567 (2008).
33. J. Jouzel et al., *Science* **317**, 793 (2007).
34. D. Pollard, R. M. DeConto, *Nature* **458**, 329 (2009).
35. T. A. Mashiotta, D. W. Lea, H. J. Spero, *Earth Planet. Sci. Lett.* **170**, 417 (1999).
36. S. C. Clemens, *Paleoceanography* **13**, 471 (1998).
37. S. J. Kim et al., *Clim. Dyn.* **31**, 1 (2008).
38. T. Kiefer, I. N. McCave, H. Elderfield, *Geophys. Res. Lett.* **33**, 027097 (2006).
39. Z. S. An, *Quat. Sci. Rev.* **19**, 171 (2000).
40. Y. J. Cai et al., *Geology* **34**, 621 (2006).
41. E. J. Rohling et al., *Quat. Sci. Rev.* **28**, 3291 (2009).
42. F. Xue, H. Wang, J. He, *J. Meteorol. Soc. Jpn.* **82**, 1173 (2004).
43. D. Fleitmann et al., *Quat. Sci. Rev.* **26**, 170 (2007).
44. C. B. Lange, W. H. Berger, H. L. Lin, G. Wefer, *Mar. Geol.* **161**, 93 (1999).
45. E. Jansen, T. Fronval, F. Rack, J. E. T. Channell, *Paleoceanography* **15**, 709 (2000).
46. A. K. Gupta, D. M. Anderson, J. T. Overpeck, *Nature* **421**, 354 (2003).
47. J. T. Overpeck, D. M. Anderson, S. Trumbore, W. L. Prell, *Clim. Dyn.* **12**, 213 (1996).
48. A. D. Vernekar, J. Zhou, J. Shukla, *J. Clim.* **8**, 248 (1995).
49. J. E. Kutzbach, P. J. Guetter, P. J. Behling, R. Selin, in *Global Climates Since the Last Glacial Maximum*, H. E. Wright et al., Eds. (Univ. of Minnesota Press, Minneapolis, 1993), pp. 24–93.
50. D. Lüthi et al., *Nature* **453**, 379 (2008).
51. J. R. Petit et al., *Nature* **399**, 429 (1999).
52. E. Kalnay et al., *Bull. Am. Meteorol. Soc.* **77**, 437 (1996).
53. R. R. Draxler, G. D. Hess, "Description of the HYSPLIT4 modeling system," National Oceanic and Atmospheric Administration (NOAA) Technical Memo, ERL ARL-224 (1997).

Supporting Online Materials
www.sciencemag.org/cgi/content/full/333/6043/719/DC1
Materials and Methods
SOM Text
Figs. S1 to S20
Tables S1 to S2
References

Science

Glacial-Interglacial Indian Summer Monsoon Dynamics

An Zhisheng, Steven C. Clemens, Ji Shen, Xiaoke Qiang, Zhangdong Jin, Youbin Sun, Warren L. Prell, Jingjia Luo, Sumin Wang, Hai Xu, Yanjun Cai, Weijian Zhou, Xiaodong Liu, Weiguo Liu, Zhengguo Shi, Libin Yan, Xiayun Xiao, Hong Chang, Feng Wu, Li Ai and Fengyan Lu

ARTICLE TOOLS	http://science.sciencemag.org/content/333/6043/719
SUPPLEMENTARY MATERIALS	http://science.sciencemag.org/content/suppl/2011/08/03/333.6043.719.DC1
RELATED CONTENT	http://science.sciencemag.org/content/sci/333/6043/706.full file:/contentpending:yes
REFERENCES	This article cites 42 articles, 2 of which you can access for free http://science.sciencemag.org/content/333/6043/719#BIBL
PERMISSIONS	http://www.sciencemag.org/help/reprints-and-permissions

Use of this article is subject to the Terms of Service